

Nao-Aki Noda^{1,*}
Hongfang Zhai¹
Kakeru Takata¹
Yoshikazu Sano¹
Yasushi Takase¹
Fei Ren²
Ryo Kawano¹
Toshihiko Umekaga¹
Yuji Yonezawa³
Hiroyuki Tanaka¹

Flow Characteristics in a Honeycomb Structure to Design Nanobubble Generating Apparatus

A nanobubble generator with honeycomb structures producing a large amount of water including large nanobubble density in a short time is described. The nanobubble-generating performance is investigated for large and small apparatus having different honeycomb cell dimensions by applying computational fluid dynamics (CFD) coupled with a population balance model (PBM). The CFD simulation shows that a significant pressure drop and shear stress occur in the bubbly flow in the honeycomb cell. The numerical model is based on the Eulerian multi-phase model and the PBM is used to calculate the bubble size distribution. The obtained CFD-PBM results are compared with the experimental results for large and small apparatus. Bubble size distributions in the honeycomb structure under different inlet absolute pressure can be predicted by the PBM. The maximum shear stress is determined as the main controlling factor for nanobubble generation.

Keywords: Computational fluid dynamics, Honeycomb structure, Nanobubbles, Population balance method

Received: August 22, 2019; *revised:* November 18, 2019; *accepted:* January 15, 2020

DOI: 10.1002/ceat.201900437

1 Introduction

In recent years, nanobubble technology has drawn great attention due to its broad applicability in wide fields of science and technology, such as life science, machinery industry, medical engineering, chemical industry, agriculture, fisheries, and civil engineering [5–8], especially focusing on washing several items, sterilization, and promoting germination. A lot of previous studies discussed microbubble generation whose diameters d are 1–100 μm [7, 9–11]. However, no detailed study is available for nanobubbles or ultrafine bubbles with diameters of $\leq 0.1 \mu\text{m}$. Therefore, in this paper, nanobubble generation mechanism and generation ability will be studied by means of numerical simulation and experiments.

This study mainly focuses on the honeycomb structure having excellent efficiency for nanobubble generation [11–14]. Tab. 1 compares nanobubble generation abilities using the honeycomb structure and Venturi tube as previously reported. As indicated in this table, although similar nanobubble densities can be obtained after 30 min, the honeycomb generator has a more than 50 times larger flow rate compared to the Venturi tube generator.

Previous visualization experiments indicated that the nitrogen bubbles in water gradually elongate and divide by going through the honeycomb cells [15–17]. Preceding computational fluid dynamics (CFD) proved that in the honeycomb structures the pressure decreases from the upstream to the down-

stream and the shear stress takes several peaks at the corners of the cells; therefore, the pressure drop and the peak shear stress may affect nanobubble generation in a large apparatus as depicted in Fig. 1a [18, 19].

In this study, a small apparatus (Fig. 1b) is newly considered for a 100-L water tank in comparison with the large apparatus in Fig. 1a used for a 1000-L water tank. In the honeycomb structures in Fig. 1c included in these apparatuses, the nanobubble-generating performance is investigated experimentally by varying the cell size. The bubble size distributions under different inlet absolute pressures are also analyzed by the

¹Prof. Nao-Aki Noda, Hongfang Zhai, Kakeru Takata, Dr. Yoshikazu Sano, Dr. Yasushi Takase, Ryo Kawano, Prof. Toshihiko Umekaga, Hiroyuki Tanaka
noda.naoaki844@mail.kyutech.jp

Mechanical Engineering Department, Kyushu Institute of Technology, Sensui-cho 1-1 Tobata-ku Kitakyushu-shi, Fukuoka, 804-8550, Japan.

²Dr. Fei Ren

School of Mechanical and Automotive Engineering, Qilu University of Technology, No. 3501, Daxue Road, Changqing, Jinan, Shandong, China.

³Yuji Yonezawa

Marufukusuisan Corp., Ltd., Kokurakita-ku Nisimoinato-cho Kitakyushu-shi, Fukuoka, Japan.

Table 1. Comparison of the nanobubble generation abilities.

	Nanofresher using the honeycomb structure by NANOX	Ultrafine GALF using the Venturi tube by IDEC
Q [L min ⁻¹]	550	16.7
p_a [MPa]	0.45	0.3
N_d after 30 min [particle mL ⁻¹]	1.7×10^8	1.42×10^8

CFD-population balance model (PBM) simulation coupled with the RNG k - ϵ turbulence model [19–21]. The final goal of this study is to design honeycomb structures generating nanobubble efficiently and to clarify the mechanism.

2 Nanobubble Generators Using Honeycomb Structures

Figs. 1a and b present schematic illustrations of the large apparatus for a 1000-L tank and the small apparatus for a 100-L tank, both of them having parallel honeycomb units immersed in water in the tank. The water and the nitrogen gas are pumped into these apparatuses together and flow into the honeycomb units. Fig. 1c shows a unit of the honeycomb structure consisting of a pair of honeycomb plates and upper and lower plates for sealing both ends. In total 16 honeycomb units are

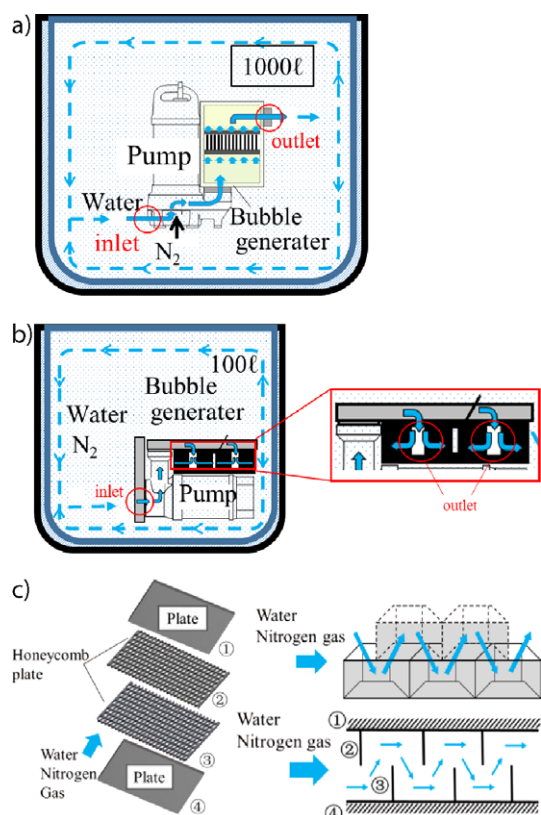


Figure 1. (a) Large apparatus including parallel 12 honeycomb units; (b) small apparatus including parallel 16 honeycomb units; (c) illustration of a honeycomb unit.

installed in the small apparatus and 12 honeycomb units are installed in the large apparatus.

In addition, Fig. 1c illustrates the nitrogen-water mixture flow through the honeycomb structure. Between each honeycomb unit, complex flow channels are formed by the overlapped honeycomb plates, in which the honeycomb

plates are shifted by $\frac{1}{2}$ cell in the flow direction. When the nitrogen-water mixture flows through the apparatus, the bubbles become finer, and the water flowing out of the generator flows into the apparatus again. This cycle is repeated, and the miniaturization effect continues [16]. Tab. 2 gives the details of the small experimental apparatus in comparison with the large apparatus used in the previous study [19]. Because the small apparatus deals with 0.1 times of the water amount of the large apparatus, a low output pump is used.

Table 2. Details of the experimental apparatus.

Item	Large apparatus	Small apparatus
Pump	Submersible pump (80TM23.7)	Submersible pump (50TMLS2.4S)
Output [kW(Hz)]	3.7 (60)	0.4 (60)
Flow rate [L min ⁻¹]	400	270
Cell size [mm]	6.1	3.9
Cell height [mm]	10	4
Cell number ^{a)}	3510	1840
Water amount [L]	1000	100
Water type	Tap water	Tap water
Gas	Nitrogen	Nitrogen
Flow rate [L min ⁻¹]	5.0	1.0
Pressure [MPa]	0.30	0.20

^{a)}Upper cell + lower cell

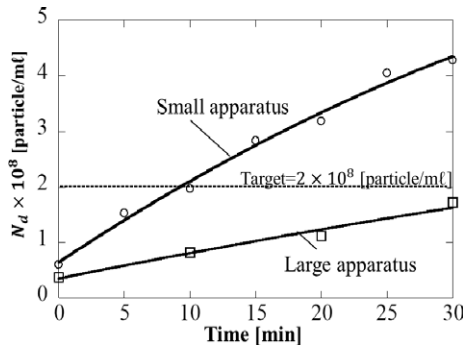
The nanoparticle analyzer Nano Sight LM10-HS is used to measure the nanobubble number density [16, 17, 22, 23]. By tracking the Brownian motion of all particles recognized on the screen and using the Stokes-Einstein equation, the particle size is obtained from the moving velocity of the particles. The nanobubble number density is measured from the collected samples under stable states after 30 min to 1 h from the experiment start where microbubbles larger than $1 \mu\text{m}$ diameter disappear.

The nanobubble generation efficiency varies depending on the different target water volume, honeycomb cell size used, and pump output. Therefore, between the small and large apparatus, the nanobubble number density per cell and per cycle will be compared.

Tab. 3 compares the experimental conditions between the large and the small apparatus. Fig. 2 shows the variation of

Table 3. Experimental conditions from the large and small apparatus.

Experimental conditions	Large apparatus	Small apparatus
Power P_w [kW]	3.7	0.4
Wall thickness [mm]	0.5	1
Pressure p_a [MPa]	0.45	0.16
Flow rate Q [L min ⁻¹]	550	103


Figure 2. Nanobubbles number density variation for large and small apparatus after the experiment start.

nanobubble number density for the large and small apparatus after the experiment starts. The nanobubble number density of the small apparatus achieves the target value after 10 min and increases further. Compared to the large apparatus, the small apparatus can achieve this aim shortly.

3 Analysis Methods

3.1 CFD for Shear Stress Distribution

All computations are performed using the commercial CFD software FLUENT 16.2. In this analysis, simplified honeycomb channels are used to realize the internal structure of the honeycomb-type bubble generator. Fig. 3 shows a three-row periodic model for large and small apparatuses. Since the results of this model are close to the results of a five-row model, in this study the former model is chosen. The dimensions of the honeycomb cells are listed in Tab. 2. At the inlet and outlet, the pressure boundary conditions are adopted. The three-row periodic model has periodic boundary conditions. The $k-\varepsilon$ model is employed to simulate the turbulent flow. The turbulent intensity $T_1^{1)}$ is expressed by [24]:

$$T_1 \equiv \frac{U_i}{U_{avr}} = 0.16(Re)^{-\frac{1}{8}} \quad (1)$$

From the Reynolds number obtained in preliminary analysis ($Re = 180-200$), the turbulent intensity is calculated as $T_1 = 10$.

1) List of symbols at the end of the paper.

At this low range of Reynolds number, the turbulent viscosity is low and does not affect the results. Also, the CFD software FLUENT16.2 uses $T_1 = 10$ as the default value.

The shear stress can be calculated as the product of strain rate and viscosity. The strain tensor e_{ij} is expressed by [25]:

$$e_{ij} = \frac{1}{2} \left(\frac{\partial U_i}{\partial x_j} + \frac{\partial U_j}{\partial x_i} \right) \quad (2)$$

This tensor has three scalar invariants, one of which is called the shear strain rate I :

$$I = \left[2 \frac{\partial U_i}{\partial x_j} e_{ij} \right]^{\frac{1}{2}} \quad (3)$$

Eq. (3) is expressed as Eq. (4) using the velocity components U_x, U_y, U_z :

$$I = \left[2 \left\{ \left(\frac{\partial U_x}{\partial x} \right)^2 + \left(\frac{\partial U_y}{\partial y} \right)^2 + \left(\frac{\partial U_z}{\partial z} \right)^2 \right\} + \left(\frac{\partial U_x}{\partial y} + \frac{\partial U_y}{\partial x} \right)^2 + \left(\frac{\partial U_x}{\partial z} + \frac{\partial U_z}{\partial x} \right)^2 + \left(\frac{\partial U_y}{\partial z} + \frac{\partial U_z}{\partial y} \right)^2 \right]^{\frac{1}{2}} \quad (4)$$

Scalar invariants in Eq. (4) are used to express shear strain rates.

Fig. 3 presents the three-row periodic model used for the large and small apparatus. For example, the small apparatus includes a honeycomb cell whose dimensions are 2.2 mm in length and 1 mm in thickness. Tab. 4 summarizes the analysis conditions of the small apparatus.

Table 4. Analysis conditions for small apparatus.

Item	Specification
Inlet absolute pressure [MPa]	0.16
Outlet absolute pressure [MPa]	0.10
Turbulent intensity [%]	10
Turbulent viscosity ratio	10

Fig. 4a illustrates the shear stress variation with the definition of Paths 1–6 in the honeycomb cell of the small apparatus. As indicated, Path 1 and 5 are located along the center of the flow path, and Paths 2, 3, 4, and 6 are along near the wall.

Fig. 4b demonstrates the shear stress variations along the vertical path z/h in Fig. 4a for the fixed distance from the wall of $d = 0.1-2$ mm. The horizontal axis z/h indicates the dimensionless distance from the bottom of the cell. The maximum shear stress τ_{max} appears near the corner as a peak value. As displayed in Fig. 4b, since the scatter of τ_{max} becomes larger for a small distance from the wall, $x = 0.1$ mm is used to show τ_{max} in the following discussion.

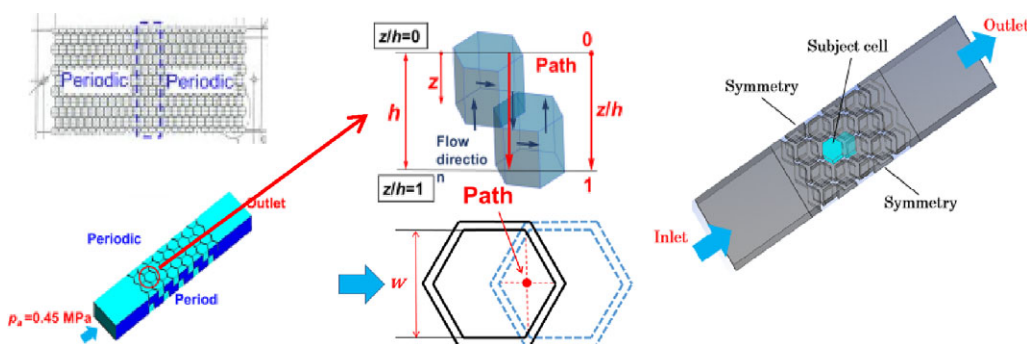


Figure 3. Periodic three-row model used for large and small apparatus.

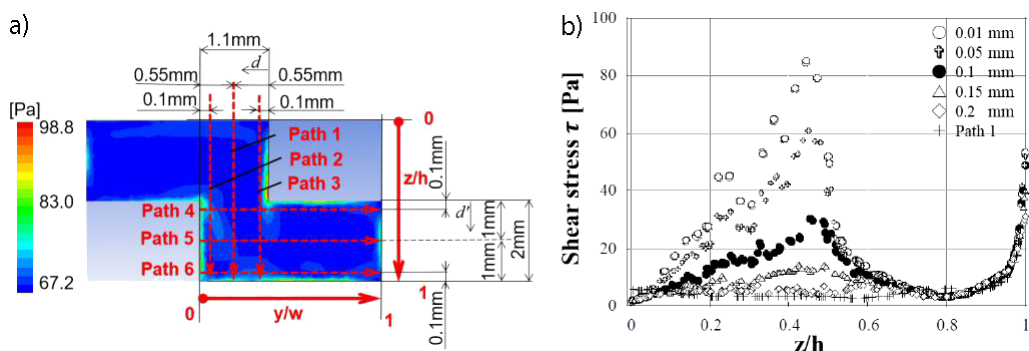


Figure 4. (a) Shear stress variation with the definition of Path1–6, (b) shear stress distribution along the path for fixed distance d from the wall.

3.2 PBM Coupled with CFD Focusing on Bubble Size Distribution

The PBM is used to simulate the nanobubble number density distribution. A progress in the CFD simulation of bubbly flow is the coupling of the PBM to CFD models, i.e., CFD-PBM coupled model [26, 27]. The PBM is for tracking the size distribution of the dispersed phase and accounting for the breakage and coalescence effects in bubbly flows [20, 21]. The analysis model is displayed in Fig. 3. The CFD-PBM analysis conditions of the small apparatus are given in Tab. 5.

Table 5. CFD-PBM analysis conditions of the small apparatus.

Item	Specification
Inlet absolute pressure [MPa]	0.16
Outlet absolute pressure [MPa]	0.10
gas volume fraction	0.00971
Initial bubble size [nm]	1280

The pressure boundary conditions are adopted. The number of bubble bins is classified into ten groups as indicated in Tab. 6 which presents diameters of bubble bins tracked in this simulation. The bin 8 specifying 1280 nm is chosen as the initial size at the inlet. The nanoparticle analyzer Nano Sight LM10-HS used in this study can detect the bubbles with diameters in the

Table 6. Diameter of each bubble bin.

Bubble bin number	Mean bubble diameter [nm]
1	10
2	20
3	40
4	80
5	160
6	320
7	640
8	1280
9	2560
10	5210

range of $x = 1-1000$ nm. The bubble bin numbers 1–7 are set within this diameter range.

The Euler-Euler two-fluid model is applied in the CFD-PBM approach [28, 29] coupled with the RNG $k-\epsilon$ turbulence model. For the bubbly flow in the honeycomb structure, the liquid is treated as a continuous primary phase and the gas as a dispersed secondary phase.

The population balance equation is written in terms of volume fraction of bubble size i :

$$\frac{\partial(\rho_p \alpha_i)}{\partial t} + \nabla(\rho_p \vec{u}_i \alpha_i) = \rho_p V_i (B_{ag,i} - D_{ag,i} + B_{br,i} - D_{br,i}) \quad (5)$$

where α_i is the volume fraction of the bubble size i which is defined as:

$$\alpha_i = N_i V_i \quad i = 0, 1, \dots, N - 1 \quad (6)$$

where V_i is the volume of the bubble size i and N_i is expressed as:

$$N_i(t) = \int_{V_i}^{V_{i+1}} n(V, t) dV \quad (7)$$

B_{ag} is called the birth rate of bubbles due to aggregation, given by:

$$B_{ag} = \frac{1}{2} \int_0^V \Omega_{ag}(V - V', V') n(V - V', t) n(V', t) dV' \quad (8)$$

D_{ag} is called the death rate of bubbles due to aggregation, given by:

$$D_{ag} = \int_0^\infty \Omega_{ag}(V, V') n(V, t) n(V', t) dV' \quad (9)$$

The birth rate of bubbles due to breakage B_{br} is defined by Eq. (10) and the death rate of due to breakage D_{br} by Eq. (11):

$$B_{br} = \int_{\Omega_v} \lambda g(V') \beta(V|V') n(V', t) dV' \quad (10)$$

$$D_{br} = g(V) n(V, t) \quad (11)$$

The breakage formulation for the discrete method in this work is based on the Hagesather method [30]. It is assumed that there is no breakage for the smallest bubble class.

4 Results of CFD Analysis

4.1 Absolute Pressure and Shear Stress Distribution

Fig. 5 indicates the absolute pressure P_a and the shear stress τ along the Paths 1–3 in Fig. 4. Figs. 5a–c present the results in the longitudinal paths and Fig. 5d–f the results in the lateral paths. The horizontal axis displays the dimensionless coordinates z/h and y/w , the vertical axis the pressure P_a and the shear stress τ along the flow path. Along the longitudinal Paths 1, 2, and 3 in Fig. 4, with increasing z/h , the pressure decreases initially and finally increases. The total pressure drop is about 0.01 along Paths 1, 2, and 3.

The maximum shear stress appears as $\tau = 30$ Pa at $z/h = 0.5$ along the longitudinal Paths 2 and 3 near the cell corner. The pressure drop and the shear stress in the longitudinal paths in Figs. 5a–c are larger than those in the lateral paths in Figs. 5d–f. The absolute pressure decreases initially and finally increases along the paths. The shear stress has a high value near the corner close to the wall, and many nanobubbles can be generated near the corner. Therefore, Path 3 is focused since it includes the maximum shear stress to compare the performance of large apparatus and small apparatus.

4.2 Comparison between the experiment and CFD results

From the experiment and fluid analysis results, the performances of the large and small apparatus are compared. Tab. 7

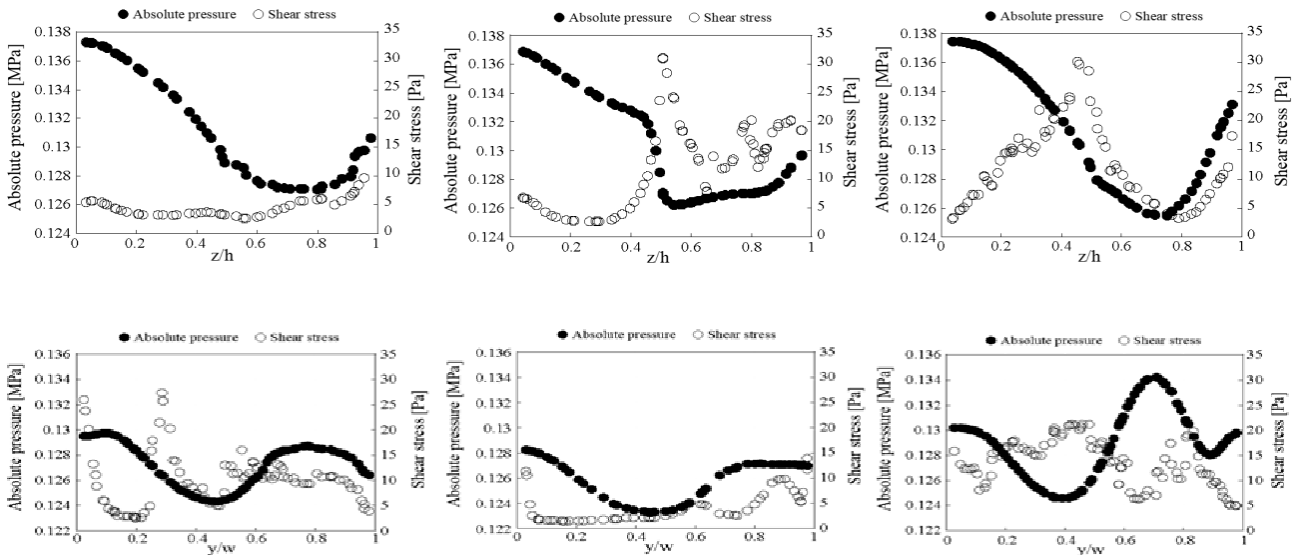
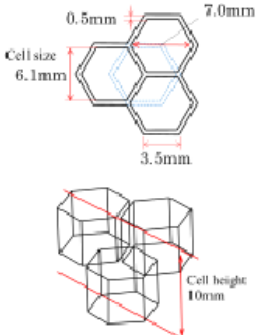
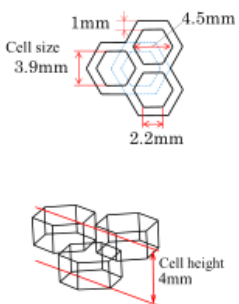


Figure 5. Absolute pressure and shear stress distribution; path (a, b, c) is longitudinal, path (d, e, f) is lateral in Fig. 4; (a) Path1 ($d = 0.55$ mm in Fig. 4); (b) Path2 ($d = 1$ mm in Fig. 4); (c) Path3 ($d = 0.1$ mm in Fig. 4); (d) Path4 ($d' = 2$ mm in Fig. 4); (e) Path5 ($d' = 1$ mm in Fig. 4); (f) Path6 ($d' = 0.1$ mm in Fig. 4).

Table 7. Comparison of nanobubble generation abilities.

Item	Large model	Small model
<i>Experimental condition</i>		
Output P_w [kW(Hz)]	3.7 (60)	0.4 (60)
Number of cells N_{cell} [-]	3510	1840
Flow rate Q [L min ⁻¹]	550	103
Water amount V [L]	1000	100
Experiment time t [min]	30	30
Number of cycle N_{cycle} [-]	33	31
<i>Experimental results</i>		
Nanobubble number density after 30min N_d^{exp} [particle mL ⁻¹]	1.7×10^8	4.3×10^8
Nanobubble number density per cell per cycle ρ_d^{exp} [particle mL ⁻¹]	3.13×10^3	7.61×10^3
<i>Cell dimensions</i>		
Honeycomb cell width w [mm]	6.1	3.9
Honeycomb cell height h [mm]	10	4

presents the experimental results of the large apparatus (Fig. 1a) and the small apparatus (Fig. 1b). Since the pump output, water amount, and honeycomb cell dimensions are different as indicated in Tab.7, the nanobubble number density per cell and per cycle are compared between the large and small apparatus.

The nanobubble number density per cell per cycle after 30 min ρ_d^{exp} is calculated from the nanobubble number density N_d^{exp} . The number of cycles of water amount N_{cycle} as defined in Eq.(12) and the total number of cells N_{cell} are given in Eq.(13).

$$N_{\text{cycle}} = (Qt)/V \quad (12)$$

$$\rho_d^{\text{exp}} = N_d^{\text{exp}} / (N_{\text{cell}} N_{\text{cycle}}) \quad (13)$$

As indicated in Tab.7, the nanobubble number density after 30 min N_d^{exp} in the large apparatus has not reached the target value of 2×10^8 particle/mL. The nanobubble number density per cell per cycle ρ_d^{exp} of the small apparatus is 2.4 times larger than that of the large apparatus.

Tab.8 compares the analysis results of the large and small apparatus along Path3. The maximum shear stress $\tau_{\text{max}}^{p_{\text{in}}=0.16} = 30$ Pa of the small apparatus is about 1.3 times larger than that of the large apparatus with 24 Pa, although the small apparatus has a lower average velocity and pressure drop.

In this study, two kinds of honeycomb cells are compared. The small apparatus has a honeycomb cell width of $w = 3.9$ mm and honeycomb cell height of $h = 4$ mm whereas the large apparatus has a honeycomb cell width of $w = 6.1$ mm and honeycomb cell height of $h = 10$ mm as indicated in Fig.3 and Tab.7. From Tab.8 it follows that with decreasing honeycomb dimension τ_{max} may increase under the same inlet pressure p_{in} . Under the same $p_{\text{in}} = 0.45$ MPa, the maximum shear stress $\tau_{\text{max}}^{p_{\text{in}}=0.45} = 56$ Pa of the small apparatus is 2.3 times larger than of the large apparatus with 24 Pa. These results demonstrate that the shear stress τ_{max} may control the nanobubble generation ability.

Table 8. Comparison of analysis results at Path3.

Item	Large apparatus	Small apparatus	
<i>Analysis condition</i>			
Inlet absolute pressure p_{in} [MPa]	0.45 (Experimental)	0.16 (Experimental)	0.45 (Equal)
<i>Analysis results</i>			
Average velocity v [$m\ s^{-1}$]	0.71	0.40	0.95
Pressure drop Δp [MPa]	0.03	0.01	0.07
Shear stress τ_{max} [Pa]	24	30	56

5 Results of CFD-PBM Analysis

5.1 Bubble Size Distribution in the Small Apparatus

The bubble size distribution in a small apparatus is simulated using CFD-PBM. Tab. 5 presents the inlet boundary condition and the pressure boundary condition of 0.16 MPa. As the outlet boundary condition, the pressure boundary condition 0.10 MPa is adopted, which is the same as atmospheric pressure. The gas volume fraction is 0.00971 at the inlet. The bin 8 specifying 1280 nm is chosen as the initial bubble size at the inlet.

Fig. 6 illustrates the nanobubble number density $N_d(x)$ in the tank, which is obtained from the CFD-PBM simulation results at the outlet $N_d^{pbm}(x)$. The simulation result $N_d(x)$ in the tank is calculated from:

$$N_d(x) = \frac{N_d^{pbm}(x)Qt}{V_{tank}} \quad (14)$$

where Q is the flow rate ($103\ L\ min^{-1}$), t is the experiment time (30 min), and V_{tank} is the volume of water in the tank (100 L). $N_d(x)$ denotes the number density of the bubbles generated from the apparatus. The original bubbles or other particles $N_d^{exp}(x)|_{t=0}$ in the water tank when $t = 0$ min are not included. The 30-min experimental result $N_d^{exp}(x)|_{t=30}$ involves the origin bubbles or other particles.

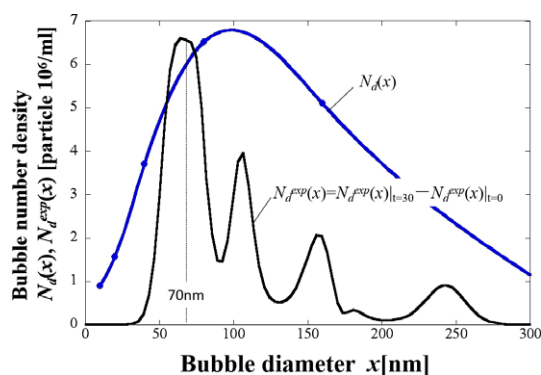


Figure 6. Bubble number density $N_d(x), N_d^{exp}(x)$ of the small apparatus in the tank.

The nanoparticle analyzer Nano Sight LM10-HS used in this study can detect bubbles within the diameter range of $x = 0-1000$ nm. As indicated in Tab. 6, the bubble bin numbers 1–7 are set within this diameter range. This is to focus on the small bubbles and to be compared with the experimental results $N_d^{exp}(x)$. Fig. 6 demonstrates that the difference is about 13% between the PBM and experimental results at 70 nm diameter. This proves that the simulation can predict sufficiently.

5.2 Maximum Shear Stress and Nanobubble Number Density Distribution under Different Inlet Absolute Pressures

The nanobubble number density $N_d(x)$ by varying the inlet absolute pressure is depicted in Fig. 7. With increasing the inlet absolute pressure, the nanobubble number density rises continuously, and the most predominant bubble size becomes larger. From the experimental results of the small apparatus, the number of bubbles diameters 70 nm is predominant. Therefore, in the following discussion, the number density of bubbles with 70 nm in diameter $N_d(70)$ is focused.

Fig. 8 presents the CFD analysis results for maximum shear stress at Path 3 by varying the inlet absolute pressure of the small apparatus. With increasing the inlet absolute pressure,

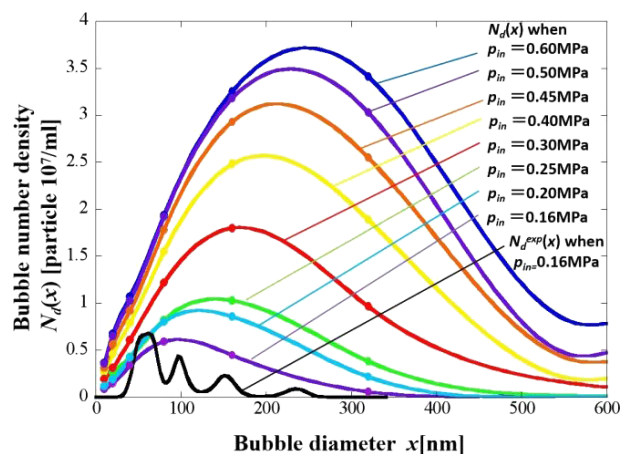


Figure 7. Bubble number density $N_d(x)$ by varying inlet absolute pressure p_{in} .

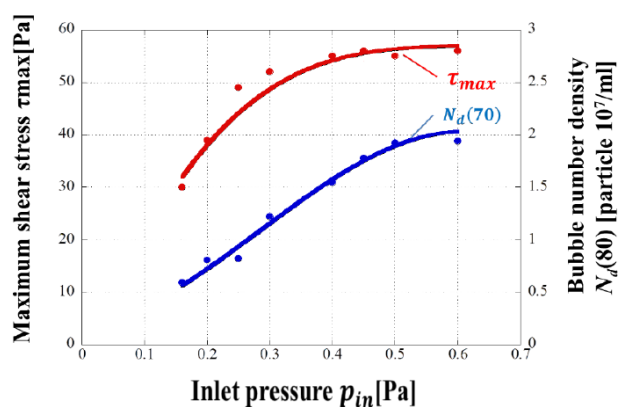


Figure 8. Maximum shear stress τ_{\max} and bubble number density $N_d(70)$ by varying the inlet absolute pressure p_{in} .

the maximum shear stress rises and is finally saturated around $p_{in} = 0.5$ MPa. Fig. 8 shows the variation of maximum shear stress and nanobubble density $N_d(70)$ by varying the inlet absolute pressure p_{in} . With increasing the inlet absolute pressure p_{in} , the maximum shear stress increases and saturates at $p_{in} = 0.4$ MPa. The density $N_d(70)$ also rises with higher p_{in} and finally saturates at $p_{in} = 0.5$ MPa.

The nanobubble number density distributions are analyzed using CFD-PBM by varying the inlet absolute pressure from $p_{in} = 0.16$ MPa to 0.6 MPa. Tab. 9 summarizes the analysis conditions when the inlet gas flow rate is fixed as 1 L min^{-1} .

Fig. 9 displays the maximum shear stress and the nanobubble density $N_d(70)$. With higher maximum shear stress, $N_d(70)$ also increases. It may be concluded that the maximum shear stress is the main controlling factor for nanobubble generation.

6 Conclusions

Several previous studies discussed the generation of micro-bubbles with diameters of $1\text{--}100 \mu\text{m}$. However, no detailed study is available for nanobubbles with diameters $< 0.1 \mu\text{m}$. Here, the nanobubble generation mechanism and generation

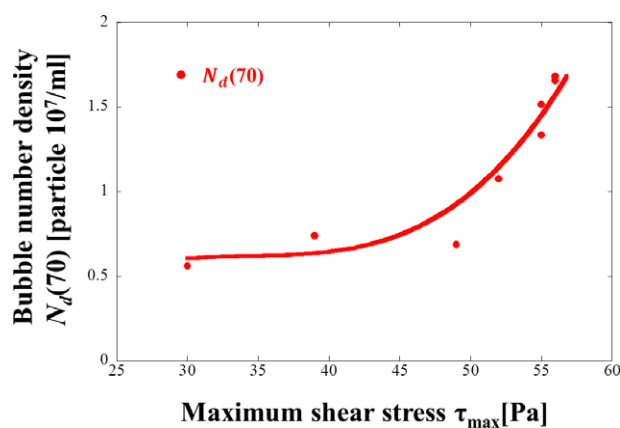


Figure 9. Bubble number density $N_d(70)$ vs. maximum shear stress τ_{\max} .

ability is studied for a small apparatus as well as a large apparatus using different honeycomb structures based on the results of experiments and CFD-PBM analysis.

(1) The maximum shear stress τ_{\max} appears at the vicinity of the honeycomb cell corner. It is for the small apparatus larger than that for the large apparatus.

(2) The experiments and the PBM analysis indicate that the nanobubble number density N_d in the honeycomb cell of the small apparatus is also higher than that of the large apparatus.

(3) The maximum shear stress is the main controlling factor for the nanobubble generation since the nanobubble number density N_d rises with increasing the maximum shear stress τ_{\max} .

Acknowledgment

This research was supported by the Ministry of Economy, Trade and Industry, METI Strategic Foundational Technology Improvement Support Operation (Heisei 26, 20140910). The authors wish to express their thanks to the group member Mr. Takahiko Ueda for his generous support to this project.

The authors have declared no conflict of interest.

Table 9. PBM analysis conditions for varying p_{in} under a fixed inlet gas flow rate of 1 L min^{-1} .

Inlet absolute pressure p_{in} [MPa]	Outlet absolute pressure [MPa]	Gas volume fraction	Initial bubble size [nm]
0.16	0.1	0.00971	1280
0.2	0.1	0.00769	1280
0.25	0.1	0.00639	1280
0.3	0.1	0.0056	1280
0.4	0.1	0.00463	1280
0.45	0.1	0.00451	1280
0.5	0.1	0.00405	1280
0.6	0.1	0.00363	1280

Symbols used

B_i	[-]	birth rate of bubbles
D_i	[-]	death rate of bubbles
E	[m ² s ⁻³]	turbulent dissipation rate
e_{ij}	[-]	strain tensor
$g(V')$	[-]	Rate of bubbles with volume V' splitting per unit time
h	[mm]	honeycomb cell height
i	[m]	bubble size
I	[-]	shear strain rate
K	[m ² s ⁻²]	turbulent kinetic energy
N_i	[-]	volume with bubble size i
N	[-]	number
N_d^{exp}	[particle mL ⁻¹]	experimental nanobubble number density
$N_d^{\text{pbm}}(x)$	[particle mL ⁻¹]	nanobubble number density obtained by PBM analysis
p_a	[MPa]	absolute pressure
p_{in}	[MPa]	inlet pressure
P_w	[kw]	power
Q	[L min ⁻¹]	flow rate
t	[s]	experiment time
T_I	[%]	turbulent intensity
U	[m s ⁻¹]	velocity
V	[m ³]	volume
V, V'	[m ³]	volume before change, volume after change
w	[mm]	honeycomb cell width
z/h	[-]	dimensionless coordinate
Δp	[MPa]	pressure drop

Greek letters

α_i	[m ³]	volume fraction
$\beta(V/V')$	[-]	probability density function bursting from volume V
λ	[-]	number of burst bubbles generated per pre-split bubble
ρ_q	[kg m ⁻³]	density of the q -th phase
ρ_d^{exp}	[m ⁻³]	nanobubble number density per cell per cycle
τ	[Pa]	shear stress
$\tau_{\text{max}}^{\text{pin}}$	[Pa]	maximum shear stress
Ω	[m ⁻³ s ⁻¹]	kernel

Sub- and superscripts

ave	average
br	breakage
ag	aggregation
max	maximum

Abbreviations

CFD	computational fluid dynamics
PBM	population balance model
RNG	renormalization group

References

- [1] K. Fukushi, Y. Matsui, N. Tambo, *J. Water SRT-Aqua* **1998**, *47*, 76–86. DOI: <https://doi.org/10.2166/aqua.1998.13>
- [2] H. Onari, T. Saga, K. Watanabe, K. Maeda, K. Matsuo, *Resour. Process. Soc. Jpn.* **1999**, *46*, 238–244. DOI: <https://doi.org/10.4144/rpsj1986.46.238>
- [3] I. Kakuta, *Bull. Soc. Sea Water Sci. Jpn.* **2006**, *60*, 160–163. DOI: <https://doi.org/10.11457/swsj1965.60.160>
- [4] H. Tsuge, *Bull. Soc. Sea Water Sci. Jpn.* **2010**, *64*, 4–10. DOI: <https://doi.org/10.11457/swsj.64.4>
- [5] M. Takahashi, *Mater. Integration* **2009**, *22*, 2–19.
- [6] K. Michioku, T. Kanda, H. Ohnari, T. Nishikawa, K. Matsuo, T. Kido, *Proc. 44th Int. Hydraulics Engineering Japan Society of Civil Engineers*, Tokyo **2000**, 1119–1118. DOI: <https://doi.org/10.2208/prohe.44.1119>
- [7] H. Hasegawa, Y. Masaki, K. Matsuuchi, Y. Yoshida, *Trans. JSME* **2006**, *72*, 160–166. DOI: <https://doi.org/10.1299/kikaib.72.2242>
- [8] *The World of Micro Bubbles* (Eds: S. Ueyama, M. Miyamoto), Kogyo Chosakai Publishing, Tokyo **2006**, 1–203.
- [9] T. Makuta, *Acoust. Soc. Jpn.* **2017**, *6*, 417–423. DOI: https://doi.org/10.20697/jasj.73.7_417
- [10] K. Mituda, *Surf. Finish. Jpn* **2017**, *7*, 331–334. DOI: <https://doi.org/10.4139/sfj.68.331>
- [11] K. Hiraki, *The Latest Technology on Microbubbles and Nanobubbles*, CMC Publishing, Tokyo **2014**, *2*, 177–183.
- [12] M. Sadatomi, A. Kawahara, K. Kano, A. Ohtomo, *Exp. Therm. Fluid Sci.* **2005**, *29*, 615–623. DOI: <https://doi.org/10.1016/j.expthermflusci.2004.08.006>
- [13] H. Tsugei, *The Latest Technology on Microbubbles and Nanobubbles II*, CMC Publishing, Tokyo **2010**, 6–10.
- [14] H. Tsuji, *Proc. 3th Int. The Japanese Society for Multiphase Flow*, Osaka **2009**, 214–215.
- [15] Y. Yonezawa et al., *Regional Innovation Creation Research and Development Project Outcome Report "Development of a Honeycomb Type Mixer for Uniformization of Nanobubbles and its Application to Industry"*, Kyushu Bureau of Economy, Trade and Industry and Kyushu Industrial Technology Center, **2012**, 2–31.
- [16] Y. Kudo, K. Hiraki, *Proc. 3th Int. The Japan Society for Design Engineering Micro-Nano Science and Technology Division*, Tokyo **2011**, 26–27. DOI: <https://doi.org/10.1299/jsmem.2011.3.129>
- [17] Y. Kudo, K. Hiraki, *Proc. National Conf. of JSME Micro-Nano Science and Technology Division*, Tokyo **2010**, *2*, 95–96.
- [18] N.-A. Noda, F. Ren, W. Yamamoto, T. Ueda, Y. Sano, D. Chen, Y. Takase, Y. Yonezawa, *Jpn. Soc. Des. Eng.* **2018**, *53*, 111–126. DOI: <https://doi.org/10.14953/jjsde.2016.2707>
- [19] F. Ren, N.-A. Noda, T. Ueda, Y. Sano, Y. Takase, T. Umekage, Y. Yonezawa, H. Tanaka, *J. Dispers. Sci. Technol.* **2018**, *40* (2), 306–317. DOI: <https://doi.org/10.1080/01932691.2018.1470009>
- [20] T.-F. Wang, J.-F. Wang, Y. Jin, *Ind. Eng. Chem. Res.* **2005**, *44*, 7540–7549. DOI: <https://doi.org/10.1021/ie0489002>
- [21] L.-M. Li, Z.-Q. Liu, B.-K. Li, H. Matsuura, F. Tsukihashi, *ISIJ Int.* **2015**, *55*, 1337–1346. DOI: <https://doi.org/10.2355/isijinternational.55.1337>
- [22] A. Malloy, B. Car, *Part. Part. Syst. Char.* **2006**, *23*, 197–204.

- [23] V. Filipe, A. Hawe, W. Jiskoot, *Pharm. Res.* **2010**, *27*, 796–810.
- [24] ANSYS®, *Academic Research*, Release16.2, ANSYS Inc.
- [25] R. Sano, *Continuum Dynamics*, Asakura Publishing, Tokyo **2007**, 46.
- [26] T. Wang, J. Wang, *Chem. Eng. Sci.* **2007**, *62*, 7107–7118. DOI: <https://doi.org/10.1016/j.ces.2007.08.033>
- [27] T. Wang, J. Wang, Y. Jin, *AIChE J.* **2006**, *52*, 125–140. DOI: <https://doi.org/10.1002/aic.10611>
- [28] D. Drew, *Annu. Rev. Fluid Mech.* **1983**, *15*, 261–291. DOI: <https://doi.org/10.1146/annurev.fl.15.010183.001401>
- [29] R. Krishna, M.-I. Urseanu, J.-M. Van Baten, J. Ellenberger, *Chem. Eng. Sci.* **1999**, *54*, 4903–4911. DOI: [https://doi.org/10.1016/S0009-2509\(99\)00211-0](https://doi.org/10.1016/S0009-2509(99)00211-0)
- [30] L. Hagesaether, H.-A. Jakobsen, H.-F. Svendsen, *Chem. Eng. Sci.* **2002**, *57*, 3251–3267. DOI: [https://doi.org/10.1016/S0009-2509\(02\)00197-5](https://doi.org/10.1016/S0009-2509(02)00197-5)

Research Article: The mechanism of nanobubble generation and generation ability are studied for a small and a large apparatus using different honeycomb structures based on the results of experiments and computational fluid dynamics/population balance model analysis. The maximum shear stress appearing repeatedly around honeycomb cell corners controls the nanobubble generation.

Flow Characteristics in a Honeycomb Structure to Design Nanobubble-Generating Apparatus

N.-A. Noda*, H. Zhai, K. Takata, Y. Sano, Y. Takase, F. Ren, R. Kawano, T. Umekaga, Y. Yonezawa, H. Tanaka

Chem. Eng. Technol. **2020**, *43* (XX), XXX ... XXX

DOI: 10.1002/ceat.201900437

